Signal Stability Studies with the Askaryan Under-Ice Radio Array

A Senior Honors Thesis

Presented in Partial Fulfillment of the Requirements for graduation *with research distinction* in Physics in the undergraduate colleges of The Ohio State University

by

Eric Suchyta

The Ohio State University
June 2010

Project Advisor: Professor James J. Beatty, Department of Physics

Signal Stability Studies with the Askaryan Under-Ice Radio Array

Eric Suchyta
The Ohio State University, Department of Physics
191 West Woodruff Ave. Columbus, OH 43210
suchyta.1@buckeyemail.osu.edu

Abstract

High energy astrophysical neutrinos are useful for understanding the origins of high energy cosmic rays, which have been a mystery for almost a century. Such neutrinos can be detected via coherent radio Cerenkov emission resulting from neutrino induced particle showers in ice. The Askaryan Under-Ice Radio Array (AURA) is an Antarctic test array of five detectors intended to study technology and analysis techniques for a future large scale radio Cherenkov neutrino array. One important input parameter for the design of such a future array is the radio frequency attenuation length in the Antarctic ice. In order to measure the ice's radio frequency attenuation length, radio signals are broadcast from a transmitter and received at the AURA detectors; by comparing the signal strength observed in two different detectors, one can measure the attenuation length. We present a preliminary stability study of extracting power signals from AURA waveforms, in preparation for the radio frequency attenuation length measurement. We define a signal extraction algorithm then proceed to determine under what conditions and to what degree a reliable power signal can be extracted. Applying the algorithm, we demonstrate good linearity for large signals and perform a statistical uncertainty exercise.

1 Introduction

1.1 High Energy Cosmic Ray Physics

The sources of high energy cosmic rays (HECRs) remain a mystery almost a century after their first discovery in 1912 by Victor Hess [1]. HECRs consist of charged particles, whose trajectories are bent by intergalactic and interstellar magnetic fields. These magnetic fields are extremely difficult to measure and are not very well known. Therefore, even when given a charged particle and the direction of its velocity vector upon reaching earth, one cannot easily backtrack the particle through the magnetic fields, back to its source [2].

In addition to the scrambling of cosmic rays in the magnetic fields, the highest energy component of the cosmic ray spectrum is attenuated. Such cosmic rays interact with the cosmic microwave background (CMB) [3] through a process known as the Greisen-Zatsepin-Kuzmin (GZK) process. For example, starting with a high energy proton:

$$p + \gamma_{\text{CMB}} \rightarrow \Delta^+ \rightarrow n + \pi^+. \tag{1}$$

For energies $\gtrsim 5 \times 10^{19}$ eV, the GZK process becomes a resonance, meaning that the interaction probability is enhanced. In fact, Greisen and Zatsepin and Kuzmin calculated that HECRs with energies $\gtrsim 5 \times 10^{19}$ eV cannot propagate distances much larger than 50 Mpc because they are too likely to collide with the cosmic microwave background [4, 5]. This means there should be a reduction in flux for very high energy cosmic rays reaching earth. Projects such as the Pierre Auger Observatory [6] and High Resolution (HiRes) Fly's Eye [7, 8] have experimentally confirmed the predicted suppression. Figure 1 plots HECR fluxes using Auger and HiRes data. There is an obvious suppression above energies of $10^{19.6}$ eV $\approx 4 \times 10^{19}$ eV $= 4$ EeV.

1.2 GZK Neutrinos

Instead of detecting HECRs themselves at earth, one may attempt to detect by products of the GZK interaction. For example, when a high energy proton collides with the cosmic microwave background according to the GZK process (see Equation 1), high energy neutrinos are produced via the following decays [9]:

$$\begin{aligned} \pi^+ &\rightarrow \mu^+ + \nu_\mu \qquad (99.98\%) \\ \mu^+ &\rightarrow e^+ + \bar{\nu}_\mu + \nu_e \qquad (100\%). \end{aligned} \tag{2}$$

These neutrinos are known as GZK neutrinos.

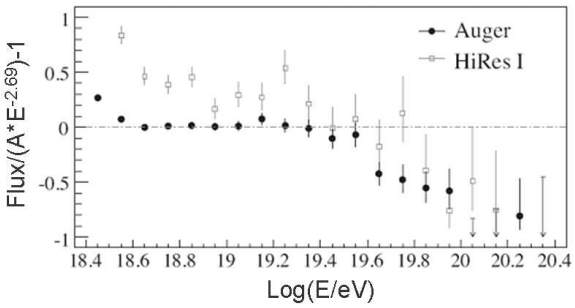

Figure 1: High energy cosmic ray spectra from the Auger and HiRes experiments. Fluxes are plotted as the fractional deviation compared to flux $\propto E^{-2.69}$. The GZK suppression is observed for energies $> 10^{19.6}$ eV $\approx 4 \times 10^{19}$ eV.

Neutrinos are uncharged, meaning their trajectories are unaffected by cosmic magnetic fields. This suggests that GZK neutrinos can be used for locating HECR sources. They will be created near the source, within a few interaction lengths of the HECR with the CMB (∼50 Mpc).

1.2.1 IceCube

IceCube [10], and its predecessor AMANDA (Antarctic Muon and Neutrino Detector Array) [11] are neutrino telescopes at the South Pole. They consist of an optical sensor array to measure neutrinos in the TeV-PeV energy scale via Cherenkov light emission of secondary particles produced in the interaction of neutrinos with the ice. Figure 2 is a schematic of the IceCube array. Each black line is an IceCube string, with 60 optical sensors along each string. IceCube instruments a volume ∼1 km^3, from depths of 1450 m down to 2450 m. Despite the enormous scale, it is inadequate to gather a large statistical sampling of neutrino energies above 100 PeV and into the GZK energy regime. The predicted GZK neutrino flux incident upon Earth is so small such that IceCube would expect to measure less than one GZK neutrino event per year [12, 13, 14]. In order to accumulate more statistics, one must build a detector which instruments a much larger volume.

A large scale increase in the optical range is unfeasible, because optical signals attenuate over short distances in the ice. Expressly, the attenuation length, defined as the distance over which a signal's amplitude decreases by a factor of $1/e$, is found to be 20-40 m for optical signals in Antarctic ice [15]. Hence, it requires many detectors to be deployed to observe a substantial effective volumes. Building and deploying the optical detectors into deep ice is not only expensive, but logistically challenging. Only a limited population can be supported at the South pole and because of the Antarctic climate, hole drilling can take place only once a year during the austral summer. Drilling takes a few days per hole, and in total, about 20 new strings per year is probably the maximum. Therefore, the prospect of significantly scaling up the IceCube experiment is not realistic.

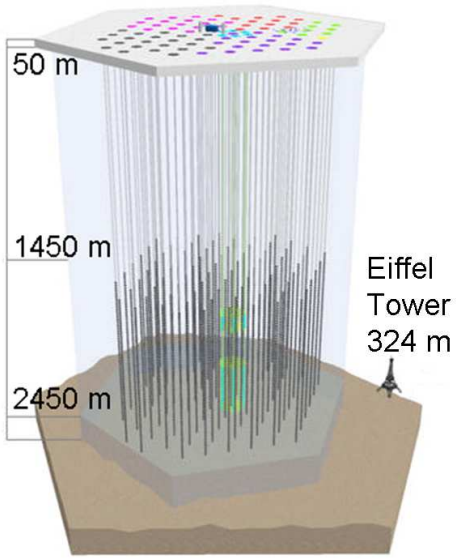

Figure 2: IceCube. Each black line is an IceCube string, consisting of 60 optical Cherenkov sensors along the string. IceCube's ∼1 km^3 scale is not large enough for GZK neutrino detection at high statistics.

1.2.2 Radio Frequency Neutrino Detection

As an alternative to optical detection, extremely high energy (∼10^{18} eV) neutrinos could also be detected in ice via the Askaryan effect. As first hypothesized by Askaryan [16, 17] in 1962, when neutrinos with energies $\gtrsim 10^{18}$ eV collide with the ice, they induce particle showers which radiate coherent radio Cherenkov emission [18, 19]. Experiments performed at SLAC in 2001 experimentally measured radio Cherenkov emission from particle showers propagating at the equivalent of that energy in ice. Radio technology is less expensive and simpler to deploy into the ice than optical technology. Moreover, radio frequency signals attenuate less over short distances in ice compared to optical signals. Broadcasting radio frequency signals down through the Antarctic ice, which reflect back from the underlying bedrock, Barwick et al. have estimated an attenuation length of ~ 1.5 km at a frequency of 380 MHz and temperature of $-50°$C [20]. This has spurred interest in a large scale radio frequency detector that could be built as an extension to IceCube because fewer detectors could be used to instrument a larger volume [21, 22]. Projects such as ARA (Askaryan Radio Array) [23] and ARIANNA (Antarctic Ross Ice Shelf Antenna Neutrino Array) [24] are under development.

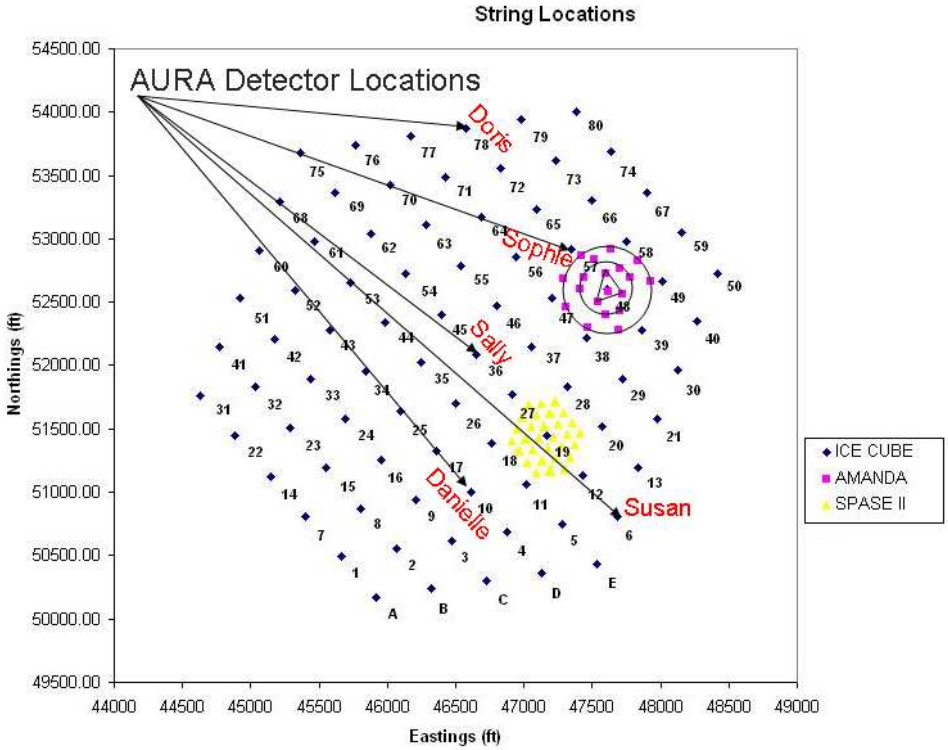

Figure 3: AURA experiment. AURA consists of five radio frequency detectors buried in the Antarctic ice, deployed among other Antarctic experiments such as IceCube, AMANDA, and SPASE II. Deep detectors are nicknamed starting with "D" (Doris, Danielle). Shallow detectors are nicknamed starting with "S" (Sophie, Sally, Susan).

1.3 AURA

The Askaryan Under-ice Radio Array (AURA) [25] is a small scale test array intended to assess technology and analysis methods for a future large scale radio Cherenkov neutrino array. AURA consists of five radio detectors buried in the Antarctic ice. Figure 3 indicates the location of the five AURA detectors relative to IceCube, AMANDA, and SPASE II [26], an air shower experiment at the South Pole. The five AURA detectors have been given nicknames according to their depth. The three detectors located at shallow depths begin with an "S"–Sophie, Sally, and Susan, and the two detectors located at deep depths begin with a "D"–Doris and Danielle.

1.3.1 The AURA Cluster

Each AURA detector is called a cluster. It consists of four dipole detector antennae, front end electronics, an Array Calibration Unit (ACU), a Digital Radio Module (DRM), and communication cables. See Figure 4. The ACU is a fifth dipole antenna, which can transmit radio frequency signals. The DRM contains the electronics for triggering, digitization, and communication. The four dipole detector antennae, called channels, are sensitive to radio frequencies ∼200-1000 MHz. Each channel contains a set of front end electronics, which filter and amplify the signals detected in the channel. Clusters trigger and read out when at least three out of the four channels detect a signal above the triggering threshold. Alternatively, clusters can be forced to read out, in what is knows as forced trigger mode. The majority of channels are functioning properly; they are listed in Table 1. However, a few need to be excluded due to hardware problems. Our analyses will not consider malfunctioning channels.

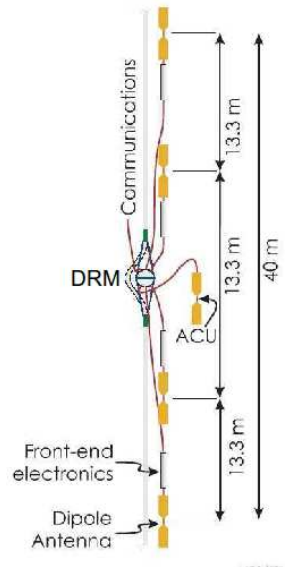

Figure 4: AURA cluster. A cluster contains four radio frequency dipole antenna detectors, one radio frequency dipole antenna transmitter (ACU), and electronics for filtering, triggering, digitization, and communication.

AURA channels are sampled at a rate of 2 GHz with a buffer length of 256 ns. Signals are recorded as a waveform of digitized counts, known as DAC (digital to analog conversion) counts. The count is 12 bit = 4096 counts, i.e. a signal height of up to $\approx \pm 2000$ DAC counts can be recorded before the channel saturates. DAC counts are converted to voltages by multiplying with a cluster dependent calibration constant. AURA hardware consists of two different technology types, one used for the deployments in 2008 (Sophie and Doris), and one used for deployments in 2009 (Danielle, Sally, and Susan). The 2008 clusters have a conversion constant of 1.08 mV/count, and the 2009 clusters have a conversion constant of 0.58 mV/count.

The front end electronics for the respective clusters also filter and amplify frequencies differently. Channels 1-4 on Doris and Susan, and channels 1-3 on Sally and Danielle are all calibrated identically and are sensitive to frequencies between 200 and 1000 MHz. Channel 4 on Sally and Danielle share a different calibration and are sensitive to frequencies between 100 and 1000 MHz. All channels in Sophie are sensitive to frequencies between 200 and 1000 MHz, but are calibrated differently than the rest of the clusters. Sophie's second and fourth channels amplify signals identically, while channels 1 and 2 each have a unique calibration. See Table 1.

2 Radio Frequency Attenuation Length Measurement

The radio frequency attenuation length in the Antarctic ice is an important design parameter for a future radio Cherenkov neutrino array because it is a contributing factor for the optimal spacing between sensors which will yield the largest effective detector volume. The AURA attenuation length calculation is a follow up to the work of Barwick et al. [20]. It is intended to expand upon their work, aiming is to precisely the radio frequency attenuation length in the ice nearby the AURA clusters. Although the AURA setup is not the ideal arrangement for an attenuation measurement, AURA can also be used as an example for further radio projects designed for a more precise measurement.

To measure the attenuation length with AURA, radio signals are broadcast from a source transmitter and detected at the different AURA clusters, with response powers P_1 and P_2 in the respective clusters. See Figure 5. The response powers are related to the attenuation length.

Two different types of source transmitters are used for AURA's attenuation length measurement:

- Cluster ACUs

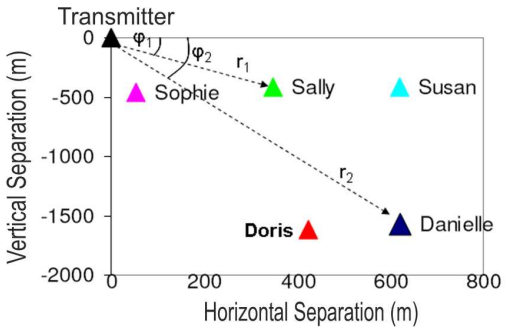

Figure 5: Attenuation measurement schematic. Radio signals are sent from a transmitter to the AURA clusters. The ratio of powers received in the clusters can be used to calculate attenuation length.

- Separate dipole antennae. Two such antennae are used, one located in the ice, nicknamed RICE (because it is from the Radio Ice Cherenkov Experiment [27]), and one located on the surface, nicknamed MAPO (because it is near the Martin A. Pomerantz Observatory).

Both the ACUs and separate antennae can transmit radio frequency signals, either as fast-rising pulses or as continuous waveforms (CW). The amplification and frequency of the transmitted signals is also adjustable. For the attenuation length calculation, it would be ideal to study both CW and pulse responses. Doing so, the systematic uncertainty could be reduced, using two different ways to measure the same quantity.

To determine the relationship between response power and attenuation length, one can use the Friis equation and write the power in a detector (P_r) as a function of distance (r), power attenuation length (λ), transmitted power (P_t), and transmitter (G_t) and detector gain (G_r):

$$P_r \propto \frac{P_t\, G_t\, G_r}{r^2}\, e^{-r/\lambda} \qquad [28,\ 29]. \tag{3}$$

λ is defined as the distance over which the transmitted signal's power decreases by a factor of $1/e$. Both the transmitter and detectors are dipole antennae, whose G_t, $G_r \propto cos^2(\phi)$, where ϕ is the angle the antenna makes with the surface. Plugging the gains into Equation 3:

$$P_r \propto \frac{P_t\, cos^4(\phi)}{r^2}\, e^{-r/\lambda}. \tag{4}$$

Considering the response powers P_1 and P_2 in two different detectors, one can use Equation 4 to write P_1/P_2:

$$\frac{P_1}{P_2} \approx \frac{r_2^2}{r_1^2}\, \frac{cos^4(\phi_1)}{cos^4(\phi_2)}\, e^{(r_2 - r_1)/\lambda}, \tag{5}$$

The transmitter power occurs in both the numerator and denominator and therefore divides out. Table 1

Table 1: AURA cluster and transmitter data needed for the attenuation length calculation. All positions are measured in IceCube coordinates.

a, b, c, d have different calibrations

Frequency ranges: a,b,c: 200-1000 MHz, d: 100-1000 MHz

Cluster Nickname	**Sophie**	**Doris**	**Sally**	**Danielle**	**Susan**
Depth Type	Shallow	Deep	Shallow	Deep	Shallow
DAC Conversion (mV/count)	1.08	1.08	0.58	0.58	0.58
Working Channels	1^a, 2^b, 4^b	1^c, 2^c, 3^c, 4^c	1^c, 2^c, 4^d	1^c, 2^c, 3^c, 4^d	4^c
x (m)	257.3	22.1	46.0	35.5	361.2
y (m)	211.6	509.5	-34.5	-365.1	-422.7
z (m) Ch 1	268.6	1423.0	229.2	1377.5	227.0
z (m) Ch 2	281.8	1436.6	240.7	1388.9	239.0
z (m) Ch 3	295.6	1451.0	249.9	1398.3	249.8
z (m) Ch 4	309.9	1462.1	261.3	1409.6	261.1
z (m) DRM	288.8	1443.7	245.2	1393.6	244.1
z (m) ACU	290.7	1445.1	247.5	1396.1	246.2
Transmitter Nickname		**MAPO**		**RICE**	
x (m)		375.4		307.3	
y (m)		97.3		194.8	
z (m)		0		176.0	

summarizes the data needed for the calculation in Equation 5.

Equation 5 is an idealized case of the attenuation length measurement. Some systematic effects also need to be considered. First, a robust attenuation length calculation needs take into account the properties of a changing medium. The index of refraction within the Antarctic ice changes with depth, meaning signals will refract [30]. Therefore, the signal will not take a completely straight path though the ice, from the transmitter to the detector, and signal ray-tracing corrections will exist for Equation 5. Simulation packages based on ray-tracing will be used in addition to Equation 5 for the final attenuation length calculation. However, Equation 5 is a first approximation adequate for our current efforts and helps when considering statistical uncertainties. Ray-tracing will add a systematic uncertainty to the attenuation length calculation.

Ray-tracing corrections to Figure 5 become most significant when the source transmitter is on the surface, because the signal must first traverse the firn, the uppermost snowy layer above the rest of the ice. The index of refraction changes more in the firn than the rest of the ice, meaning that ray-tracing effects are larger in the firn than the rest of the ice [30]. This will make the ultimate attenuation length calculation more difficult for data whose source transmitter is located on the surface. To avoid possible complication, our preliminary studies have focused on data from sources within the ice.

In addition to ray-tracing, cable shadowing adds another systematic uncertainty to the attenuation length calculation. The location of communication cables running from the surface to the detectors is not known; it is difficult to determine where cables settle after deployment. The cables could absorb some amount of signal, thus affecting the attenuation length calculation.

Similarly, the positions and angular orientation of the dipole antennae cannot be determined exactly. Uncertainties in the geometry also contribute to the systematic uncertainties in the attenuation length measurement. Equation 5 assumed all antennae had an identical angular orientation, with the axis of maximum gain parallel to the surface. Otherwise, there would not be a $\cos^4(\phi)$ term. There would be four separate $\cos^2(\phi)$ terms, each with a different angle.

If r_1 and r_2 in Equation 5 are too close together, r_2-r_1 in the exponential becomes small and λ has little effect; i.e. there is little effect due to attenuation. Hence, for the attenuation length measurement, it is best to consider one shallow and one deep cluster. Identifying clean signals in both shallow and deep clusters turns out not to be so simple. When signals look clean in the deep clusters, the shallow clusters tend to saturate, and when signals look clean in the shallow clusters the signals in the deep clusters tend to be very small.

Clearly, the attenuation length measurement depends on reliably extracting power from the signals received at the AURA clusters. Prior to the measurement, we must make sure that extracted signals are stable. We will develop a method of how to define a power signal and how to check its stability. Our analyses then focus on the performance of this signal extraction. We check linearity and perform a statistical uncertainty exercise.

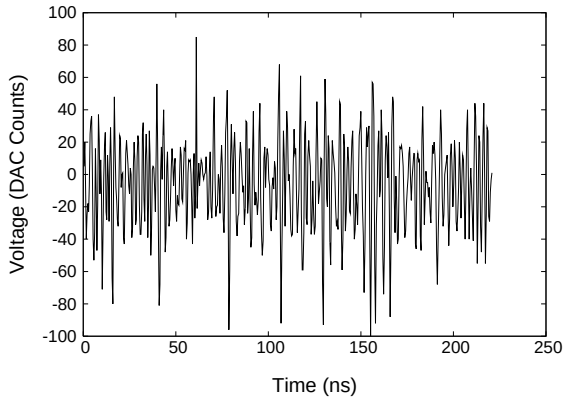

(a) Forced trigger response in Sophie.

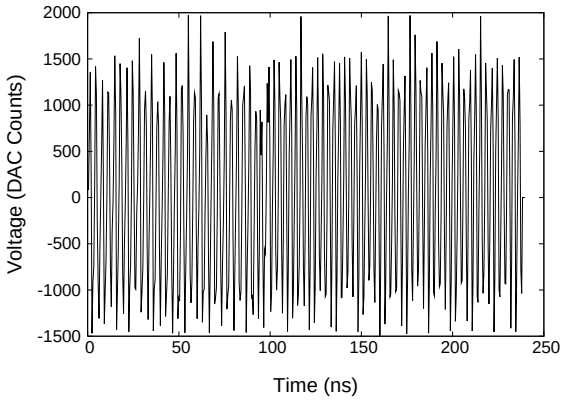

(b) Sally, using RICE transmitter set as 300 MHZ CW source.

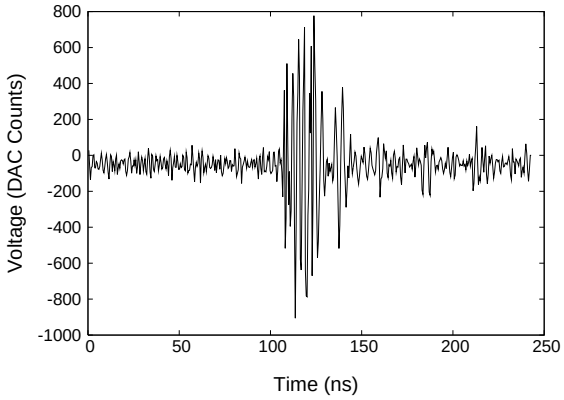

(c) Danielle, using RICE transmitter set as fast-rising pulse source.

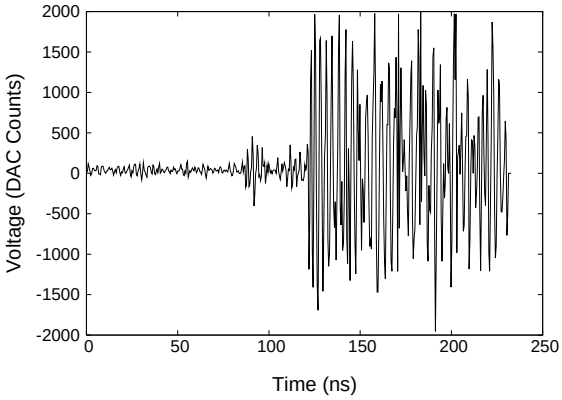

(d) Saturated response in Sally, transmitter with same settings as Figure 6(c) above. The response's shape does not look like Figure 6(c) above

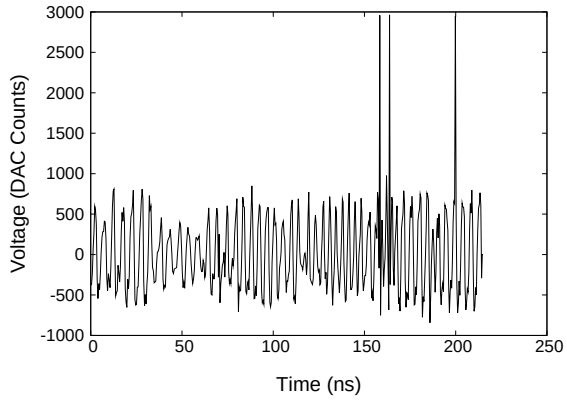

(e) Sophie, using RICE transmitter set as fast-rising pulse source. This response is not characteristic of fast-rising pulse and cannot be physical.

Figure 6: Examples of single waveform AURA cluster responses

3 Signal Extraction

Next, we present and evaluate a number of AURA signals. We then explain the analyses we apply for our studies. For the sake of clarity and brevity, unless otherwise indicated, we will restrict our attention and only present plots from channel 1 in the clusters. Additional plots will be uploaded to the related website [31].

3.1 AURA Signals

The plots in Figure 6 are examples of signals received at the AURA clusters. Figure 6(a) is an example of a forced trigger readout. Figures 6(b)-6(d) use the RICE transmitter as the signal source. In Figure 6(b) the transmitter is set to 300 MHz CW, and in Figures 6(c)-6(e) the transmitter is pulsing. Figures 6(a) and 6(e) are from Sophie, Figure 6(b) and 6(d) are from Sally, and Figure 6(c) is from Danielle.

The response in Figure 6(d) saturates. (Although this example if for a pulsing transmitter, saturation could occur for CW as well.) The highest readings should actually be higher than 2000 DAC counts. However, the cluster's hardware cannot count any higher. Moreover, the shape of the signal in Figure 6(d) also does not look characteristic of a fast-rising pulse. Certainly, it looks very different from Figure 6(c). By the end of the buffer window, the signal height has been very large for a duration of over 100 ns, and does not appear to be dying out, indicating that clusters respond differently to saturated signals.

3.1.1 Data Cleanup

The response in Figure 6(e) does not look at all characteristic of a fast-rising pulse. In fact, it looks more like a wave. Furthermore, there are even enormous peaks above the maximum DAC count level. Such a response cannot be physical. Signals such as Figure 6(e) are filtered out before any further analyzes.

3.2 CW and Pulse Analyses

CW signals have the advantage that the source transmitter is tuned to a definite frequency, allowing one to characterize a CW signal received at an AURA cluster by a spike in the cluster's frequency response near the transmitter frequency. Frequency responses are computed by taking the Fast Fourier Transform (FFT) of the time response. Details about performing the FFTs will be discussed in the following Fast Fourier Transform section.

Figure 7(a) corresponds to Figure 6(b)'s frequency response, which indeed exhibits the expected peak near 300 MHz. Figure 7(b) on the other hand corresponds to Figure 6(c)'s frequency response. Frequency responses for a pulsing transmitter exhibit no such peak, because the transmitter broadcasts a range of frequencies.

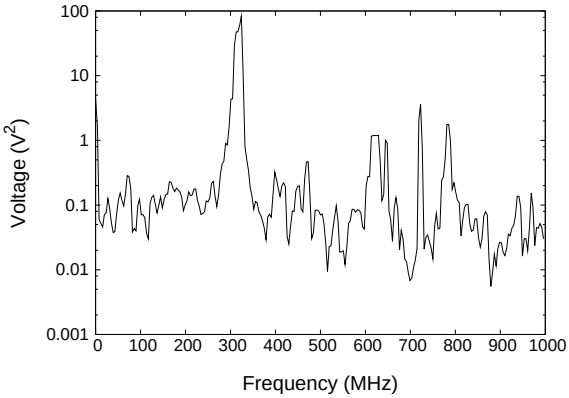

(a) Sally, using RICE transmitter as 300 MHZ CW source. Characterized by peak near transmitter frequency.

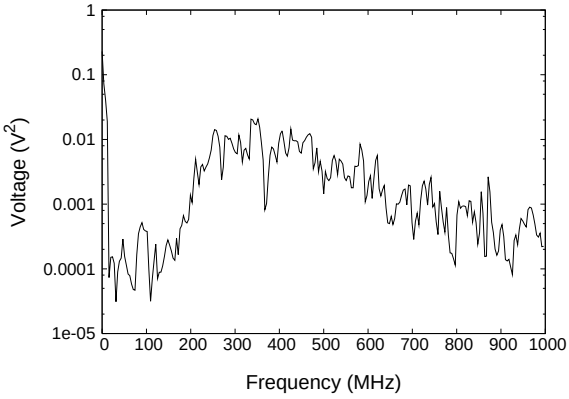

(b) Danielle, using RICE transmitter as fast-rising pulse source. Characterized by range of transmitter frequencies.

Figure 7: Examples of single waveform frequency responses

3.2.1 Timing Correction

The raw data taken by AURA needs to be corrected in order to obtain the waveform. A timing correction is applied, which uses two different sampling speeds [32]. Somewhere within the waveform (but different for every waveform), the time increment, dt, between subsequent voltage readings changes, because the sampling speed changes. After the timing correction, neither of the dts is required to equal the 0.5 ns that a 2 GHz sampling alone would yield. This effect can be seen in Figure 6. One may notice that Figure 6's time axes do not extend as high as 256 ns, the buffer length, because the timing correction has been applied to the waveform.

3.2.2 Fast Fourier Transform

Figure 7(a) uses the sampling speed correction. Doing so is needed before performing the FFTs. When a constant sampling speed is assumed over the entire waveform, Figure 7(a) becomes Figure 8. The bimodal peak near 300 MHz is not an effect we expect physically.

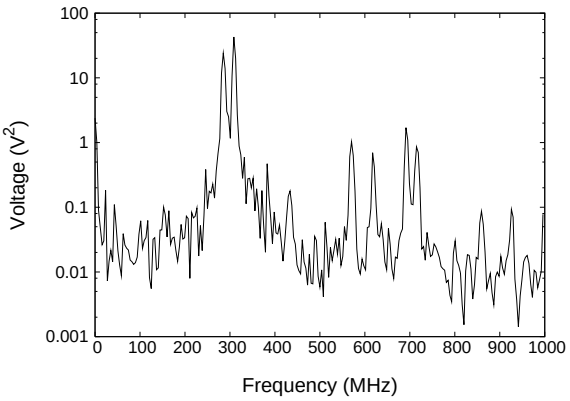

Figure 8: Example of a single waveform frequency response in Sally before applying the sampling speeds corrections, RICE transmitter at CW frequency of 300 MHz. The bimodal peek near the transmitter frequency would not be expected physically.

The algorithm for using the two different sampling speeds when performing the FFTs is to split the signal where the sampling speed changes, FFT each piece separately, and then recombine. Signals are split into two pieces by checking where in the waveform the dt between voltage readings changes. When dt changes, the signal is divided. We then have two separate waveforms, each with a different number of samples. An FFT is performed on each of these waveforms independently, resulting in two frequency responses with different discrete frequencies. The two waveforms are recombined into a single waveform with 256 evenly spaced samples, spanning 0-1000 MHz. Doing so is analogous to rebinning histograms. Each of the 256 frequencies is the center of a bin. One then integrates the two independent waveforms over a bin and divides by the bin size, to determine the size of the recombined waveform in that bin. Following this procedure, the bimodal peak merges into a single peak, and one recovers Figure 7(a).

3.3 Data Acquisition

AURA data is acquired in different operation modes. The standard operation mode is a physics runs. Here the detector looks for transient signals. Triggering occurs when an AURA cluster detects a signal above triggering threshold in at least three out of four of its channels.

We are using test calibration runs. Such runs last ∼1-10 minutes, exporting ∼ 1000 waveforms per cluster per channel. We denote triggered readout as an event. The settings for the source transmitter remain constant over the entire run duration, allowing us to average the ∼1000 events. This defines a single waveform which represents the channel's response over the run.

We consider two different types of calibration runs:

- Forced trigger runs. All source transmitters are turned off, and the AURA clusters operate in forced trigger mode. Such runs are useful for analyzing pedestal.
- Transmitter runs. Source transmitter broadcasts a nonzero signal, and the clusters trigger normally.

3.4 Data Analysis

3.4.1 Forced Trigger Runs

By averaging a cluster's frequency response over several forced trigger runs, we estimate radio frequency pedestal levels in that cluster. Figure 9 plots average pedestal waveforms for Sally, Danielle, Sophie, and Doris. Susan is excluded because only one of the four channels functions properly.

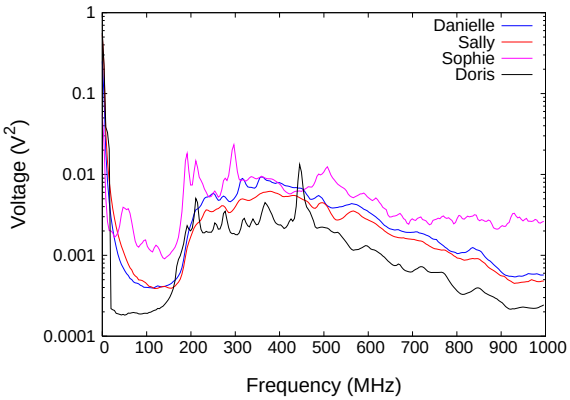

Figure 9: Average pedestal responses forcing the detectors to read out.

3.4.2 Pulser Transmitter Runs

Pulser runs have been challenging to analyze due to the variety of different signal types seen in the different clusters. As explained in the Attenuation Length section, it is important to consider the attenuation length calculation between one shallow and one deep cluster. The signal needs to be large enough to be seen in the far sensor. However, the near sensor then saturates. This can be seen in Figure 6(d), using Sally and the RICE transmitter. Saturation corrections would need to be applied to such responses before extracting a power from the signal. However, doing so would add another uncertainty to the final attenuation length calculation.

Sophie's response for the same run is very different. Most of the events look rather strange, like

Figure 6(e). Such events are filtered out, and doing so leaves few events after data cleanup. A few events for this run look do look similar to Figure 6(c), for example Figure 10. However, the amplitude is much smaller, low enough that it is not easy to identify the signals from noise. Accordingly, it is also difficult to determine the time interval which contains the signal. It is not readily evident at which times the signal begins and ends. This further complicates trying to extract powers from such signals.

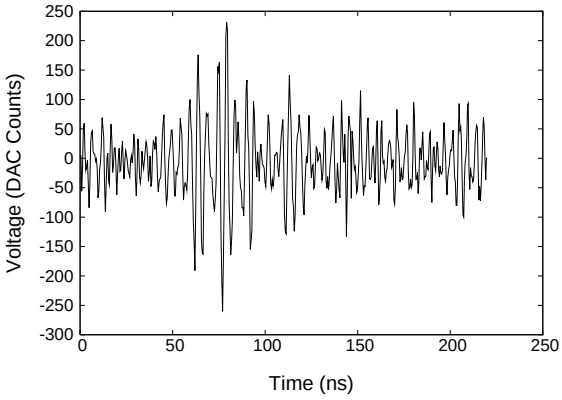

Figure 10: Occasionally RICE pulser responses in Sophie look physical. (Most look like Figure 6(e).) However, such signals have small amplitudes and are difficult to distinguish from pedestal.

3.4.3 Pulser Discussion

Due to the difficulties in Sally and Sophie, identifying good pulse signals in the shallow clusters, using the RICE transmitter has proved very challenging. Susan is not especially helpful because only one of the four channels is functioning properly. We have focused on the RICE runs because, the attenuation calculation is more difficult for the surface pulser source, and the runs which use cluster ACUs as a pulser are more recent such that we have not been able to thoroughly evaluate them yet. We are currently working to do so.

An attenuation calculation using the pulse data would proceed much like the recent acoustic measurement using the South Pole Acoustic Test Setup (SPATS) [33]. Upon identifying what time interval contains the true signal, one adds the signal squared over this interval to compute the power. The problem here lies in defining these intervals, because the shapes of the AURA signals can be very different. Signals may need to be normalized in some way to account for the different responses. For the time being, the CW analyses offer a more viable alternative for the attenuation calculation.

3.4.4 CW Transmitter Runs

Figure 11 plots the average waveforms over one run in Sally, for the RICE transmitter tuned to 300 MHz. In addition to the 300 MHz peak, one sees secondary peaks at higher frequencies, which look like higher order harmonics. However, all the secondary peaks are not at integer multiples of the first peak where higher harmonics should occur. The affect is not fully understood.

Figure 11 indicates that channel 3's response is significantly smaller than the response in the other channels. It is one of the channels which is not working properly. Channel 4's response is also somewhat smaller. However, the difference is due to the difference in calibration between channel 4 and the other three channels. It is not a functionality problem.

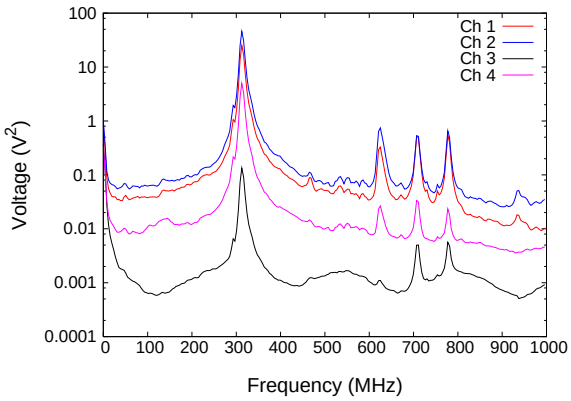

Figure 11: Sally, average signal in each channel over the ∼1000 waveforms in one run. RICE transmitter set to 300 MHz. Channel 3's response is low because it is malfunctioning. Channel 4 is lower than Channels 1 and 2 due to calibration differences.

3.4.5 CW Power Extraction Analyses

The proposed algorithm for extracting powers from a CW signal is to integrate the average frequency domain signal in a small window near the transmitter frequency. The intent is that the signal to noise ratio should be maximized within this window. In order to optimally extract reliable signals, one must identify reasonable limits for the frequency window. Moreover, in order to determine the uncertainty on the extracted powers, one must evaluate the uncertainty upon summing the signal over the window. The uncertainty in the extracted powers is essential when discussing the uncertainty of the attenuation length. We proceed along these lines, analyzing a number of signals, with a focus on evaluating uncertainty and identifying a suitable integration window. Doing so we investigate under what conditions and to what degree a reliable power extraction, and therefore attenuation calculation can be performed.

To evaluate uncertainty, we calculate variances. Since transmitter runs consist of ∼1000 events, we can compute not only the average of the signal at each frequency, but also the variance at each frequency. Therefore, we can evaluate how much a cluster's fre-

quency response fluctuates over the course of a run.

In general, variance is defined by:

$$\sigma^2 = \sum_{i=1}^{N_{events}} \frac{(x_{avg} - x_i)^2}{N_{events}}. \quad (6)$$

Here x_i corresponds to an event's response at frequency, f, and x_{avg} corresponds to the average response over the run at f. N_{events} is the number of events in the run. For a run, we calculate two separate variances at each f, both an upper and a lower variance. We do so because the two variances turn out to be asymmetric. At each f, a particular event's response amplitude may either be higher or lower than the run average at that f. All the runs lower than average at f are used to calculate the lower variance at f, and all the runs higher than average at f are used to calculate the upper variance at f. Symbolically:

$$\sigma^2_{f,lower} = \sum_{i=1}^{N_{lower}} \frac{(x_{avg} - x_i)^2}{N_{lower}} \quad (7)$$

$$\sigma^2_{f,upper} = \sum_{i=1}^{N_{upper}} \frac{(x_{avg} - x_i)^2}{N_{upper}}. \quad (8)$$

Figure 12 plots the average signal in Sally for a run during which the RICE transmitter is adjusted to 500 MHz. Figure 12, includes $\sigma_{f,lower}$ and $\sigma_{f,upper}$ as lower and upper uncertainty bars. For clarity, we have zoomed in on the frequency range 200-800 MHz, and plotted the error bars for every third frequency. Except Figure 12 for illustration, we do not plot errors bars on more of the figures to follow in order to preserve readability.

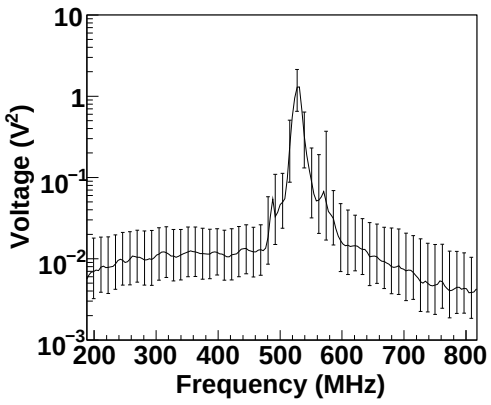

Figure 12: Average signal over one run for Sally, including variances over the run. (Uncertainties are only plotted at third point to maintain clarity.) RICE transmitter set to 500 MHz. Power will be calculated by integrating this plot in some window around the peak.

Figure 13 shows Sophie's frequency response for three different RICE transmitter frequency settings, 300, 500, and 700 MHz. These are the three common frequency setting for CW runs. The plots indicate that the received signal strength decreases as the transmitter frequency increases. This general trend is observed in all the clusters. By the 700 MHz transmitter frequency, there is no longer a significant peak, high above the rest of the signal near the transmitter frequency. Figure 13 suggests one must be careful when considering higher frequency CW runs. Often times they will not be sufficiently far above pedestal to make a contribution toward a meaningful attenuation calculation. For the remainder of the section, we will concentrate on 300 and 500 MHz CW signals.

One may also notice in Figure 13 (or in previous figures) that peaks in frequency response are slightly offset from the transmitter frequencies. Here the response peaks are at about 320, 530, and 740 MHz for 300, 500, and 700 MHz transmitter settings. The effect comes from the AURA electronics and not the transmitter. However, the effect is not a large concern because we can define the integrating window around the response peak, even if it is slightly offset from the transmitter frequency.

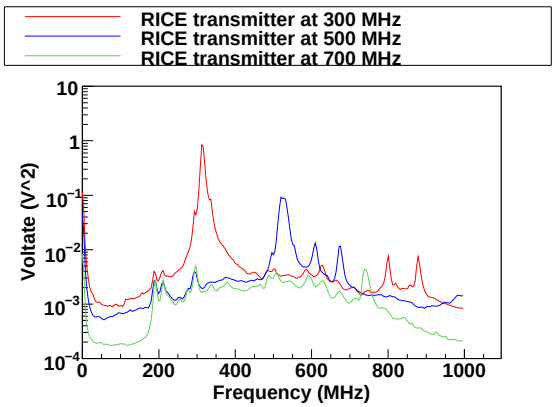

Figure 13: Sophie average frequency responses for RICE transmitter frequencies of 300, 500, and 700 MHz. The peak near the transmitter frequency for the 700 MHz response is small, and will not be suitable for the attenuation length calculation. There is a small shifting of peak frequencies–response peaks are at about 320, 530, and 740 MHz for 300, 500, and 700 MHz transmitter settings. Power integrals will be defined around the response peaks.

Computing the signal to pedestal ratio is a useful quantity when considering the integrating window. Figure 14 plots how Sally's signal compares to the Sally's pedestal in Figure 9. The RICE transmitter is adjusted to 500 MHz for the black waveform and 300 MHz for the green waveform. Consider the region which extends 30 MHz left of one of the peaks, up to 30 MHz right of the peak. In both the waveforms, the signal is far above the pedestal within this region. Such features are typical of the AURA signal to pedestal plots. Hence we have preliminarily defined the integrating window's endpoints to begin and end 30 MHz to either side of the peak.

One notices obvious bumps near these endpoints. However, the bumps may not be any real effect, and may just be some kind artifact or fluctuation. We do not attempt to assign any physical significance to the bumps. What matters most is (as it will become apparent below) that the window we have defined for the extraction will yield reasonable extraction.

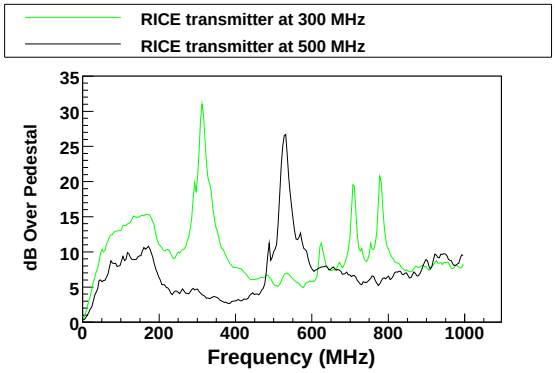

Figure 14: Sally, average signal to pedestal plots for RICE transmitter set to 300 and 500 MHz. The endpoints for the power integral have preliminarily been defined 30 MHz left and 30 right of the peaks.

It is also useful to plot the two waveforms from Figure 14 separately, then add additional waveforms with the same transmitter frequency, but different transmitter power. Figure 15 plots runs for three different nonzero RICE transmitter powers, when the transmitter's frequency is held constant at 300 MHz. Defining the first run as the 0 dB transmitter power, the second run's transmitter power is 6 dB higher, and the third run's transmitter power is 12 dB higher. Figure 15 indicates that the response at frequencies outside the integrating window is also higher for larger transmitter amplitudes. For example, consider the region below 200 MHz. Sally channel 1 is not sensitive to frequencies under 200 MHz, meaning that the responses below 200 MHz are caused by noise in the electronics. Although it is not the case here, in addition to electronics noise, higher order harmonic effects can also contribute to changing the shape of the response at frequencies greater than the transmitter frequency. Only in the absence of such effects should one expect the signals at frequencies outside the integrating window to have the same response amplitude.

Figure 15 is also helpful as a quick, rough check as to whether the runs are scaling reasonably. In the integrating window, one expects that the signals should be offset by approximately 6 dB, the separation between the transmitters. Here, the peaks occur near 14 dB, 20 dB, and 26 dB respectively.

However, it is not the peaks alone which need to be considered. The proposed algorithm for extracting power from the signals was to integrate over a window of 60 MHz centered on the peak frequency. Thus, the proper question to ask is if the the three integrals

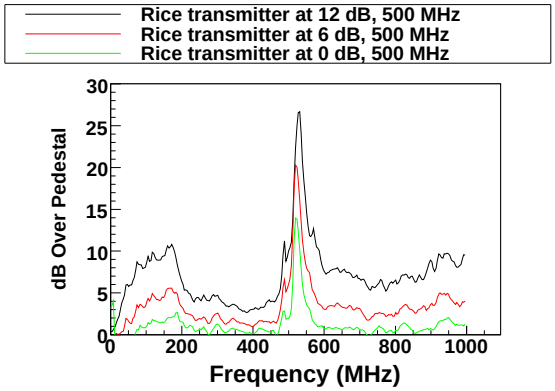

Figure 15: Sally, scaling for three different RICE transmitter power settings, 0, 6, 12 dB, at a frequency of 500 MHz. As expected the peaks are offset by approximately 6 dB. The response below 200 MHz is electronics noise.

over the window scale according to 0, 6, and 12 dB offsets. For example, Figure 16 plots runs for the same three transmitter power settings as Figure 15, but the transmitter's frequency has been changed to 500 MHz. The peak for the 12 dB run is not as far as 6 dB over the 6 dB run, but it turns out the summed scaling over the integrating window will look as expected.

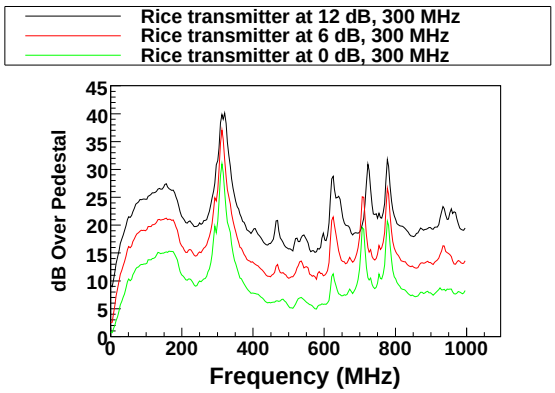

Figure 16: Sally, scaling for three different RICE transmitter power settings, 0, 6, 12 dB, at a frequency of 300 MHz. Although the black and red peaks are not 6 dB apart the powers will be seen to scale reasonably upon integrating.

Having identified the integrating window and defined the calculation for the uncertainty at each frequency over a run, we proceed to calculate the power, P, for a run, including its uncertainty. Here it is useful to refer back to Figure 12. The power is simply the summation of all the n points between the window endpoint frequencies. The lower and upper variances in P, δP_{lower} and δP_{upper} are then found by adding

in quadrature each $\sigma_{f,lower}$ or $\sigma_{f,upper}$:

$$P = \sum_{i=1}^{n} x_{avg} \tag{9}$$

$$\delta P^2_{lower} = \sum_{i=1}^{n} \sigma^2_{f,lower} \tag{10}$$

$$\delta P^2_{upper} = \sum_{i=1}^{n} \sigma^2_{f,upper}. \tag{11}$$

δP_{lower} and δP_{upper} correspond to the lower and upper uncertainty limits in P.

The results of calculating Equations 9, 10, and 11 for various runs are plotted in Figure 17. The red dots correspond to Sally for the three runs in Figure 16–RICE transmitter frequency set to 300 MHz; the blue dots correspond to Sally for the three runs in Figure 15–RICE transmitter frequency set to 500 MHz; and the green dots correspond to Doris for these same three runs 500 MHz runs. Powers are calculated in dB, compared to a reference offset of 100 V^2. The colored curves drawn are lines of slope 1. For signals sufficiently far above the pedestal, we expect the powers should scale linearly with the transmitter's power. Both the 500 and 300 MHz power sets for Sally agree with the respective scaling curves. However, the power set for Doris does not agree with the corresponding scaling line. The powers are all about the same size, meaning that very little (if any) signal is reaching Doris.

Figure 17 suggests that as long as a large enough signal reaches a cluster, the power extraction algorithm's linearity holds reasonably well. Furthermore, we can use the uncertainty to estimate what the statistical uncertainty will look like for Equation 5. Propagating the error according to Equation 5:

$$\delta\lambda_s = \frac{r_2 - r_1}{\left(ln\left[\frac{P_1}{P_2}\frac{r_1^2}{r_2^2}\frac{cos^4(\phi_2)}{cos^4(\phi_1)}\right]\right)^2}\sqrt{\left(\frac{\delta P_1}{P_1}\right)^2 + \left(\frac{\delta P_2}{P_2}\right)^2}. \tag{12}$$

Thus far, we have only seen CW signals sufficiently above pedestal in the shallow clusters. Nevertheless, Equation 12 is in fact useful for estimating $\delta\lambda_s$ given a transmitter and any two clusters. Repeating the power extraction algorithm for additional runs $\frac{\delta P}{P}$ is typically $\lesssim 30\%$, for both Sally and Sophie. The $\lesssim 30\%$ is using δP_{upper}, the larger of the two asymmetric uncertainties, for δP. It is questionable to make any definitive statements about δP using Susan, because only one of the four channels is functioning properly. Furthermore, as can be seen in Figure 17, the upper error bars in Doris, a deep cluster, appear to be similar in size to the upper error bars in Sally, a shallow cluster. This relationship should not be taken too seriously since little signal is being received at

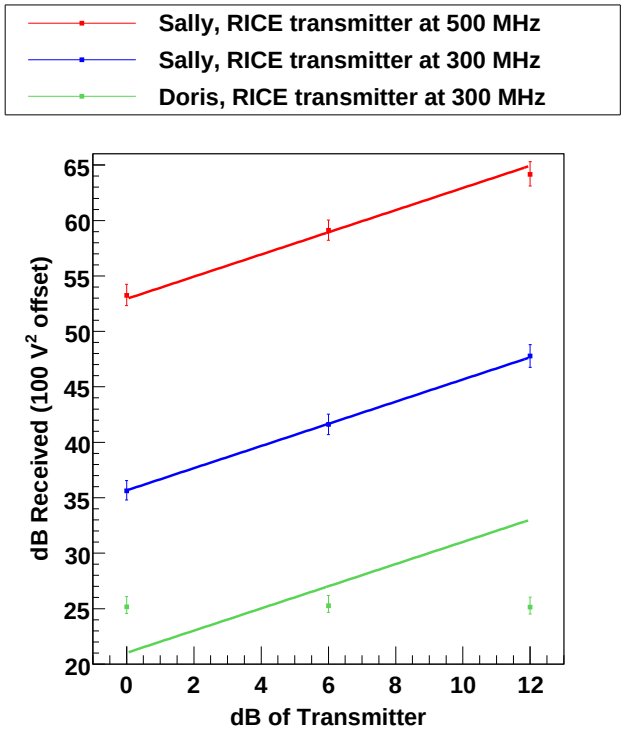

Figure 17: Calculating powers and their uncertainties for various runs, at 0, 6, and 12 dB power settings for the RICE transmitter. The colored curves are the expected scaling for a signal well above pedestal. The power extraction works well for signals well above pedestal, and the error bars will allow for estimating uncertainties in the attenuation length measurement.

Doris. However, it is reasonable to assume, especially for clusters with identical hardware, that clusters will have at least approximately equal relative statistical errors when measuring large enough signals within the DAC count limit. For example, Sally and Danielle have identical hardware, so we would expect them to make approximately the same relative errors when measuring appreciable signals. Thus the $\lesssim 30\%$ is a useful first approximation for what can be expected in general for $\frac{\delta P}{P}$. Expecting λ somewhere near 750 m according to [20], Equation 5 can be solved for $\frac{P_1}{P_2}$, then $\frac{P_1}{P_2}$ can be plugged into Equation 12 to estimate $\delta\lambda_s$ given a transmitter and two clusters. Using the RICE in-ice dipole transmitter, Sally, and Danielle, $\delta\lambda_s \approx 200$ m, approximately 25% of 750 m. We can also adjust the $\frac{\delta P}{P}$ in Danielle, and see what effect it has on $\delta\lambda_s$. For example, if $\frac{\delta P}{P}$ was closer to 50%, $\delta\lambda_s$ grows to ≈ 300 m.

Equation 12 demonstrates that the geometric relationship between cluster and transmitter locations can play a big role in the size of the statistical uncertainty $\delta\lambda_s$. For example using Susan's ACU as the transmitter, Sally, and Sophie, $\delta\lambda_s$ of over 1.5 km, twice λ itself is to be expected. Such case is an example quantifying how for the attenuation length measurement, one does not want to consider two clusters which are too close together.

As previously mentioned, there are systematic effects due to ray-tracing, cable shadowing, and antennae orientation which will affect the attenuation length calculation. These will add systematic uncertainties in λ to consider. The combination of systematic and statistical uncertainty makes up the total $\delta\lambda$.

3.4.6 CW Plans

Currently we are evaluating some newer runs in order to determine potentially useful deep cluster runs. Many of these runs are using cluster ACUs as the source transmitter. We would like to find clean signals in at least one of the deep clusters, because then we will be able to achieve smaller statistical errors in the attenuation length measurement according to the arguments above. In addition to the runs already taken, more test run data from Antarctica can still be taken if need be.

We can improve upon Figure 17 by adjusting the width of the integrating window, and taking note if the plot changes at all. Doing so is a way to further check stability. Furthermore, we can consider noise subtraction routines, such as sideband techniques. For example, in Figure 15 responses outside the integrating window, e.g. near 400 or 700 MHz, give some indication of noise levels, including both background and electronics.

4 Conclusion

High Energy astrophysical neutrinos can be used for locating HECR sources. AURA is currently studying the prospect of radio frequency Cherenkov detection of high energy neutrinos in the Antarctic ice. The radio frequency attenuation length of the Antarctic ice around such a detector is an important future design parameter, and we have presented an initial study of the stability in the signals associated with the attenuation length measurement using AURA test data.

5 Acknowledgments

I would like to thank Carsten Rott (The Ohio State University) for his continued assistance, both with the project itself and writing this Honors Thesis. I would also like the thank the members of the Beatty Research Group (The Ohio State University) for their assistance throughout the course of my work. I thank Hagar Landsman (University of Wisconsin) and Dave Besson (Kansas University) for various AURA related correspondences. Finally, I would like to thank the committee members, Jim Beatty (The Ohio State University, Physics), Richard Hughes (The Ohio State University, Physics), and Jennifer Johnson (The Ohio State University, Astronomy) for serving on my Honors Thesis committee.

References

[1] VF Hess. Observations of the penetrating radiation on seven balloon flights. *Phys. Z.*, 13:1084, 1912.

[2] Yun-Ying Jiang, L. G. Hou, X. H. Sun, Wei Wang, and J. L. Han. Possible Sources of Ultrahigh Energy Cosmic Ray. 2010.

[3] Arno A. Penzias and Robert Woodrow Wilson. A Measurement of excess antenna temperature at 4080- Mc/s. *Astrophys. J.*, 142:419–421, 1965.

[4] Kenneth Greisen. End to the Cosmic-Ray Spectrum? *Phys. Rev. Lett.*, 16:748–750, 1966.

[5] G. T. Zatsepin and V. A. Kuz'min. Upper Limit of the Spectrum of Cosmic Rays. *JETPL*, 4:78–80, 1966.

[6] J. Abraham et al. Observation of the suppression of the flux of cosmic rays above 4×10^{19}eV. *Phys. Rev. Lett.*, 101:061101, 2008.

[7] R. Abbasi et al. Observation of the GZK cutoff by the HiRes experiment. *Phys. Rev. Lett.*, 100:101101, 2008.

[8] R. U. Abbasi et al. Measurement of the Flux of Ultra High Energy Cosmic Rays by the Stereo Technique. *Astropart. Phys.*, 32:53–60, 2009.

[9] C. Amsler et al. (Particle Data Group), PL B667, 1 (2008) and 2009 partial update for the 2010 edition (URL: http://pdg.lbl.gov).

[10] M. Ackermann et al. The ICECUBE prototype string in AMANDA. *Nucl. Instrum. Meth.*, A556:169–181, 2006.

[11] J. Ahrens et al. Muon Track Reconstruction and Data Selection Techniques in AMANDA. *Nucl. Instrum. Meth.*, A524:169–194, 2004.

[12] V. S. Beresinsky and G. T. Zatsepin. Cosmic rays at ultrahigh-energies. *Phys. Lett.*, B28:423–424, 1969.

[13] Ralph Engel, David Seckel, and Todor Stanev. Neutrinos from propagation of ultra-high energy protons. *Phys. Rev.*, D64:093010, 2001.

[14] Hasan Yüksel and Matthew D. Kistler. Enhanced cosmological GRB rates and implications for cosmogenic neutrinos. *Phys. Rev. D*, 75(8):083004, Apr 2007.

[15] M. Ackermann et al. Optical properties of deep glacial ice at the South Pole. *J. Geophys. Res*, 111:D13203, 2006.

[16] G.A. Askaryan. *JETP*, 14:441, 1962.

[17] G.A. Askaryan. *JETP*, 21:658, 1965.

[18] J. Alvarez-Muniz, R. A. Vazquez, and E. Zas. Calculation methods for radio pulses from high energy showers. *Phys. Rev.*, D62:063001, 2000.

[19] J. Alvarez-Muniz and E. Zas. Cherenkov radio pulses from EeV neutrino interactions: The LPM effect. *Phys. Lett.*, B411:218–224, 1997.

[20] S. Barwick, D. Besson, P. Gorham, and D. Saltzberg. South Polar in situ radio-frequency ice attenuation. *J. Glaciol.*, 51:231–238, 2005.

[21] P. Allison et al. IceRay: An IceCube-centered Radio-Cherenkov GZK Neutrino Detector. *Nucl. Instrum. Meth.*, A604:S64–S69, 2009.

[22] Pisin Chen and K. D. Hoffman. Origin and evolution of cosmic accelerators - the unique discovery potential of an UHE neutrino telescope: Astronomy Decadal Survey (2010-2020) Science White Paper. 2009.

[23] Shang-Yu Sun, Pisin Chen, and Melin Huang. Simulation of the Event Reconstruction of Ultra High Energy Cosmic Neutrinos with Askaryan Radio Array. 2010.

[24] Steven W. Barwick. ARIANNA: A New Concept for UHE Neutrino Detection. *J. Phys. Conf. Ser.*, 60:276–283, 2007.

[25] H. Landsman, L. Ruckman, and G. S. Varner. AURA - A radio frequency extension to IceCube. 2008.

[26] J. E. Dickinson et al. The new South Pole air shower experiment: SPASE-2. *Nucl. Instrum. Meth.*, A440:95–113, 2000.

[27] Jenni Adams and Suruj Seunarine. The RICE Experiment. Slides presented at 18th International Workshop on Weak Interactions and neutrinos (WIN02), 21-26 Jan 2002, Christchurch, New Zealand.

[28] G. B. Rybicki and A.P. Lightman. Radiative Processes in Astrophysics. ISBN: 0471048151.

[29] J. D. Jackson. Classical Electrodynamics. ISBN: 047143132X.

[30] I. Kravchenko et al. *Astropart. Phys.*, 20:195, 2003.

[31] `http://wiki.icecube.wisc.edu/index.php/Aura_attenuation_new`.

[32] Private communication with Hagar Landsman.

[33] Delia Tosi and for the IceCube Collaboration. Measurement of Acoustic Attenuation in South Pole Ice. *arXiv:1004.1694*, 2010.